



Effects of source model variations on Coulomb stress analyses of a multi-fault intraplate earthquake sequence

Hiwa Mohammadi^{a,*}, Mark Quigley^a, Sandy Steacy^b, Brendan Duffy^a

^a School of Earth Sciences, The University of Melbourne, Victoria 3010, Australia

^b School of Physical Sciences, The University of Adelaide, South Australia 5005, Australia

ARTICLE INFO

Keywords:

Intraplate earthquakes
Multi-fault earthquakes
Tennant Creek sequence
Stress transfer
Coulomb stress changes

ABSTRACT

Fault models are quickly produced and iteratively improved over weeks to years following a major earthquake, to characterise the dynamics of rupture, evaluate the role of stress transfer, and contribute to earthquake forecasting. We model Coulomb stress transfer (Δ CFS) between the largest foreshock (Mw 5.4; 1 year prior to first mainshock) and three Mw 6.1 to 6.5 earthquakes that occurred in a 12-hour period on January 22, 1988 in central Australia (Tennant Creek earthquake sequence) to investigate the role of static stress transfer in earthquake triggering relative to progressive source model development. The effects of fault model variance are studied using Δ CFS modelling of five different fault source model sequences (27 total models) using different inputs from seismic and geospatial data. Some initial models do not yield positive Δ CFS changes proximal to hypocentres but in all models, preceding earthquakes generate positive Δ CFS (≥ 0.1 bar) on ≥ 10 to 30% of the forthcoming receiver fault rupture areas. The most refined and data-integrative model reveals Δ CFS $\geq +0.7$ to $+13$ bars within 2 km of impending hypocentres and large (≥ 30 to 99%) areas of positive Δ CFS. When compared to global compilations of threshold Δ CFS prior to impending ruptures (average = 3.71 bar, median = 1 bar), this suggests that Coulomb stress change theory adequately explains the Tennant Creek rupture sequence. In the most-refined model, earthquake inter-event times decrease as Δ CFS increases, suggesting that higher stress magnitudes may have more rapidly (within hours) triggered successive events, thus accounting for some temporal aspects of this sequence. Δ CFS analyses provide a useful framework for understanding the spatiotemporal aspects of some intraplate earthquakes. The progressive refinement of source models using emergent data may reduce epistemic uncertainties in the role of stress transfer that result from different model inputs, approaches, and results.

1. Introduction

Multi-fault earthquakes and earthquake sequences are common in many tectonic settings on Earth (e.g., Sieh et al., 1993; Fletcher et al., 2016; Wei et al., 2011; Beavan et al., 2012; Elliott et al., 2012; Hamling et al., 2017; Quigley et al., 2019; Clark et al., 2012). Distinct fault ruptures may be triggered as part of a quasi-continuous cascading seismic moment release, or be triggered seconds, minutes, hours, days, or even decades following preceding earthquakes (Belardinelli et al., 2003a, 2003b; Freed, 2005; Nissen et al., 2016; Stein, 1999). Stress changes due to moderate-to-large earthquakes may affect the location of subsequent events by processes including static stress transfer, dynamic (i.e., coseismic) stress changes and viscoelastic stress change (e.g., King et al., 1994; Stein, 1999; Nostro et al., 1997; Reasenberg and Simpson, 1992; Stein et al., 1997; Lin and Stein, 2004; Steacy et al.,

2013). The relative importance of these different types of stress changes in earthquake sequences may be challenging to evaluate as they all may provide scientifically valid explanations for aspects of the same sequence. Static stress changes estimated from Coulomb stress calculations (e.g., Harris and Simpson, 1998) have been shown to provide an important explanation for some instances of earthquake triggering and clustering (e.g., King et al., 1994; Harris, 1998; Stein, 1999; Harris et al., 1995; Freed and Lin, 2001; Freed, 2005; Steacy et al., 2005; Mohammadi and Bayrak, 2015; Mohammadi et al., 2017) by suppressing or encouraging rupture on receiver faults. Coulomb stress change analysis may be a potentially powerful forecasting tool if it can be reliably applied to rapidly-developed fault models (Steacy et al., 2014).

Although the calculation of Coulomb stress changes is well-established, the early stages of many earthquake sequences see the emergence of multiple diverse models for fault ruptures that vary in fault

* Corresponding author.

E-mail address: mohammadih@student.unimelb.edu.au (H. Mohammadi).

<https://doi.org/10.1016/j.tecto.2019.06.007>

Received 28 February 2019; Received in revised form 7 June 2019; Accepted 8 June 2019

Available online 12 June 2019

0040-1951/ © 2019 Elsevier B.V. All rights reserved.

geometries and co-seismic slip due to different modelling approaches and utility of different datasets (e.g., seismological data, geologic data, optical data, InSAR, geodetic data). Model variations impart significant epistemic uncertainty to interpretation of the relationships between stress transfer and earthquake sequencing (Wang et al., 2014; Zhan et al., 2011). Changing parameters of the Coulomb stress change model, including the stress change tensor (related to changing geometries and slip distributions of the source fault), receiver fault geometry, and the friction coefficient and Skempton's coefficient, may impact on how well static stress change analyses explain observation of spatiotemporal patterns of earthquake sequences (Lin and Stein, 2004; Zhan et al., 2011; Wang et al., 2014; Mildon et al., 2016). Fault model uncertainties are rarely applied to stress-triggering studies; although some studies have examined uncertainties in receiver fault geometries (e.g., Harris and Simpson, 2002; Steacy et al., 2005; Lasocki et al., 2009). Woessner et al. (2012) conducted a thorough analysis of the effects of fault model uncertainties on Coulomb stress models for the moment magnitude (M_w) = 5.9 June 2000 Kleifarvatn earthquake in southwest Iceland.

Another limitation of many Coulomb stress change studies is the ambiguity with which estimated stress changes on receiver faults are interpreted to have been enough to trigger rupture. A Coulomb stress increase of 0.01 MPa (0.1 bar) is commonly proposed to be the threshold for potential earthquake triggering (Harris, 1998; Reasenber and Simpson, 1992; Freed, 2005; King et al., 1994; Stein, 1999). However, the stress threshold to trigger instantaneous rupture on receiver faults concurrent with the hypocentral source fault rupture may be significantly higher. For example, Coulomb stress changes of > 0.1 MPa (Zhan et al., 2011) and 1 to 1.5 MPa (Walters et al., 2018) were insufficient to generate spontaneous rupture during the 2010–2011 Canterbury earthquake sequence and 2016 Central Italy seismic sequence, respectively. Instead subsequent receiver fault ruptures occurred days (Walters et al., 2018) to months (Zhan et al., 2011) after initial stress loading from prior mainshocks.

In this paper, we apply Coulomb stress modelling to investigate the rupture behaviour of the 1987 to 1988 Tennant Creek earthquake sequence in Australia. We aim to investigate (1) whether static stress changes on receiver faults induced by preceding earthquakes provide an explanation for the observed spatiotemporal patterns of this sequence, including the hypocentral locations and inter-event timing, and (2) whether differences in fault geometry and rupture kinematics (associated with different rupture models), influence static stress changes significantly enough to cast uncertainty over whether Coulomb stress models adequately explain this sequence. We also consider maximum calculated stress change increases on receiver faults in the context of stress triggering thresholds and time lags between source and receiver fault ruptures for this and other earthquake sequences globally.

2. Seismotectonics of the 1987–1988 Tennant Creek earthquake sequence

The Australian continent moves north relative to the ITRF 2014 NNR model (Altamimi et al., 2017) at 6.7 cm/yr but accommodates little internal strain (Tregoning, 2002). Australia has a complex intraplate stress field that reflects interactions amongst plate tectonic forces exerted from distant plate boundaries (Hillis et al., 2008) with local stress perturbations associated with faults, lithological density and strength contrasts and intraplate volcanism (Rajabi et al., 2017 and references therein). Seismicity occurs in concentrated zones and more dispersed regions across the continent, with an average of two earthquakes $M_w \geq 5$ per year, and abundant evidence for historical and prehistoric (paleo-seismic) surface ruptures in earthquakes of M_w 5.4 to ≥ 6.6 (Crone et al., 1997; Quigley et al., 2006, 2010; Clark et al., 2012, 2014; King et al., 2018) (Fig. 1A). Several historical earthquakes exhibit highly complex surface rupture traces (King et al., 2018 and references therein) that suggest rupture of multiple faults during a single earthquake (e.g., 2016 Petermann earthquake; King et al., 2018) or multiple

earthquakes (e.g., 1988 Tennant Creek sequence; Bowman, 1988).

The Tennant Creek area in Australia's Northern Territory is approximately 1500 km from the nearest plate boundary. Based on historical and instrumental reports, no earthquakes larger than magnitude 5 were reported within 500 km of Tennant Creek between European arrival (late 1800s) and 1987. The Warramunga (WRA) array (Fig. 1b), which is located 30 km east of the Tennant Creek epicentral area, was installed in 1965 (Bowman, 1988). The L-shaped array of vertical component broad-band seismometers in shallow boreholes includes 20 elements at approximately 2.5 km spacing supplemented by 4 additional sites (Fig. 1B).

A local magnitude (ML) 4.1 earthquake occurred in the Tennant Creek area in February 1986, however, no further earthquakes ≥ 3 were recorded between February 1986 and January 1987. The 1987–1988 Tennant Creek earthquake sequence began with a series of six teleseismically recorded earthquakes that occurred between January 5 and 9, 1987 with body wave magnitudes (Mb) of 4 to 5.2 (e.g., Choy and Bowman, 1990, Bowman and Dewey, 1991; Bowman, 1991). There are no published source mechanisms or slip distribution models for any of these events with the exception of the January 9, 1987 magnitude Mb 5.2 (M_w 5.4) (Bowman and Dewey, 1991) earthquake (forthwith referred to as the largest foreshock; LFS).

On January 22, 1988 at 10:06 a.m. Australian Central Standard Time, a Mw 6.2 (Mb 6.1, ML 6.3) earthquake (TC1) generated strong regional shaking near the 1987 sequence. A Mw 6.3 earthquake (Mb 6.1, ML 6.4) earthquake (TC2) occurred about 3.5 h after TC1. A Mw 6.6 earthquake (TC3; Mb 6.5, ML 6.7) occurred 12.5 h after TC1 and 8 h after TC2. Collectively, these earthquakes created a ~ 32 km surface rupture (Bowman, 1988; Bowman et al., 1990a, 1990b; Jones et al., 1991). The maximum intensity experienced in Tennant Creek region from these earthquakes was MM VII (Jones et al., 1991). Relevant data for each of these earthquakes is shown in Table 1.

Epicentre locations, hypocentral depths, magnitude estimates, and fault plane solutions for the Tennant Creek main shocks were published by Harvard CMT, USGS, ISC, Geoscience Australia (GA) and others (e.g., McCaffrey, 1989, Bowman and Dewey, 1991). The variance in epicentre locations is shown in Fig. 1B and Table 1. Relocations of the Tennant Creek main shocks using refined seismic velocity models and aftershock locations were determined using the WRA seismic array and a provisional network of portable seismographs installed 2 days after TC3 (Bowman, 1988; Bowman et al., 1990a). Foreshocks, mainshocks, and aftershocks (until July 1990) within $\sim 1^\circ$ of the Tennant Creek mainshock locations were relocated by Bowman and Dewey (1991) (Fig. 1C). McCaffrey (1989) relocated main shocks using teleseismic long period P and SH and short period P waves and produced a three-fault model for the 1988 sequence (Fig. 1B, Tables 2 and 3). Choy and Bowman (1990) analysed the broadband teleseismic records and produced fault models for three events and largest aftershock. They used three subevents to find best fitting solution for each main shock. For TC1 and TC3, all three-subevents had the same geometry and kinematics, however, for TC2, the two first subevents had the same kinematics and geometry but the 3rd subevent fault was different. Additionally, Leonard et al. (2002) compiled data and produced p wave first solutions, with preferred fault planes based on field observations from Jones et al. (1991).

The relocated positions of the largest foreshock and TC 1–3 (Bowman and Dewey, 1991), show that these events are restricted to the western part of the fault zone, between the Kunayungku and Lake Surprise scarps. The Tennant Creek main shocks produced 32 km of surface faulting on at least two main scarps, the Kunayungku, WLS and ELS fault (Fig. 1a) (Bowman, 1988). Bowman et al. (1990a) argue that the TC1 formed the Kunayungku scarp, TC2 formed the western Lake Surprise scarp and TC3 produced the eastern Lake Surprise scarp (Bowman, 1988) (the order of the scarps has been shown in Fig. 1C). Relocated epicentres of the 1988 main shocks show that TC 1–3 hypocentres moved progressively from west to east across the fault zone

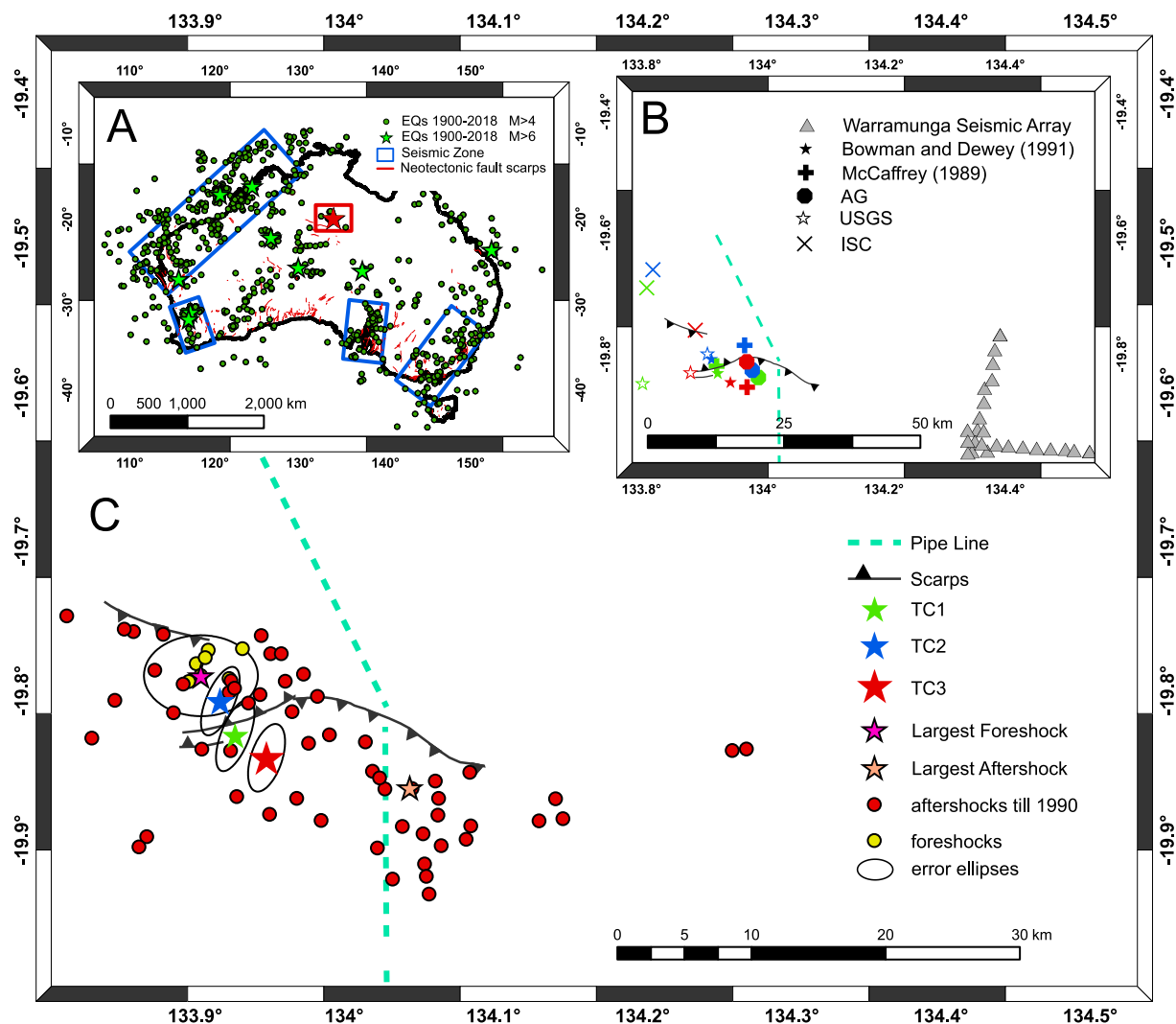


Fig. 1. A) Earthquake epicentres (Green dots) $M \geq 4$ (1900–2018) and seismic zones (Blue rectangles) of elevated seismicity from Hillis et al. (2008), red rectangle indicates the Tennant Creek area and Red lines show neotectonics features (e.g., fault scarps). B) Different epicentres from different sources (green ones for first Tennant Creek main shock (TC1), Blue ones for Second Tennant Creek main shock (TC2) and Red ones for third Tennant Creek main shock (TC3). C) Relocated epicentres with confidence ellipse semi-axes < 8 km in length by Bowman and Dewey (1991). Black line are the scarps with ticks on hanging-wall side, numbers 1–Kunayungku; 2 and 3 – West and East Lake Surprise (boomerang shape) and dashed green line is Gas pipe line. (For interpretation of the references to color in this figure legend, the reader is referred to the web version of this article.)

(Bowman, 1988; Bowman, 1991). The distribution of scarps relative to relocated hypocentres suggests that the foreshock activity might relate to a segment boundary on pre-existing faults.

The scarp morphology and excavations through the Kunayungku, WLS and ELS scarps (Bowman et al., 1990a, 1990b; Crone et al., 1992; Jones et al., 1991) demonstrate primarily thrust-reverse faulting, consistent with the majority of moment release in teleseismic fault plane solutions (Choy and Bowman, 1990; McCaffrey, 1989). The southern side of the Kunayungku and ELS scarps is upthrown. The northwestern side of the WLS scarp is upthrown. Choy and Bowman (1990) and McCaffrey (1989) suggest TC1 ruptured from the hypocentre toward the surface and the northwest, while rupture during the TC3 propagated horizontally toward the southeast (Choy and Bowman, 1990). The focal mechanisms of TC1 and 3, together with the aftershock distribution, are consistent with reverse faulting on planes dipping to the south-southwest. TC2 was associated with complex teleseismic waveforms and showed no resolvable rupture directivity (Bowman, 1991) but McCaffrey, 1989 suggest that the TC2 ruptured bi-laterally. Some teleseismic sub-events and the p-wave fault plane solutions suggest strike-slip components and rupture complexity during TC2 (McCaffrey, 1989;

Choy and Bowman, 1990; Bowman, 1992; Jones et al., 1991). The orientation of the fault scarps and the opposite sense (south-vergent) of displacement, suggests an overall complex geometry of faulting when viewed as a composite record of TC 1–3. Bowman (1991) used surveying levelling data together with field observations and seismologic data to develop a series of fault models with uniform slip on rectangular, dip-slip faults for TC 1–3. His preferred model comprises three faults in a conjugate array (Table 3).

3. Coulomb stress change calculations: theory

One of the most straightforward and powerful physics-based methods to forecast the distribution of triggered seismicity is Coulomb stress change modelling (Rybicki, 1973; Smith and Van de Lindt, 1969; Stein, 1999; Toda and Stein, 2003; Toda et al., 2005). This method is successful in forecasting locations of aftershocks, with accuracy that improves as seismic network density increases and slip inversions become more accurate. In this study we focus on static stress changes, although other sources of stress such as dynamic stress changes (e.g., Kilb et al., 2000; Gomberg et al., 2001; Felzer and Brodsky, 2005, 2006)

Table 1
Occurrence times, and hypocentre locations (from different sources) of Tennant Creek sequence.

		Foreshock (LFS)	TC1	TC2	TC3
Date and time	Day	9	22	22	22
	Month	1	1	1	1
	Year	1987	1988	1988	1988
	TIME (H:M) UTC	11:27	3:57	3:57	12:04
AG	Depth (KM)	10	6	4	5
	Latitude (°)	-19.968	-19.812	-19.826	-19.838
	Longitude (°)	133.738	133.975	133.984	133.994
USGS	Depth (KM)	5	5	5	5
	Latitude (°)	-20.11	19.847	19.79	19.829
	Longitude (°)	133.636	133.803	133.91	133.882
Harvard CMT	Depth (KM)		15	15	15
	Latitude (°)		-19.69	-19.66	-19.76
	Longitude (°)		133.81	133.82	133.89
ISC	Depth (KM)	5	5	5	5
	Latitude (°)	-20.0881	-19.8247	-19.781	-19.803
	Longitude (°)	133.6631	133.8569	133.924	133.951
Bowman and Dewey (1991)	Depth (KM)	6.6	6.5 ± 1.0	3.5 ± 0.5	4.5 ± 0.5
	Latitude (°)	-19.79	-19.83	-19.807	-19.845
	Longitude (°)	133.904	133.927	133.917	133.948
McCaffrey (1989)	Depth (KM)		2.7	3	4.2
	Latitude (°)		-19.84927536	-19.808	-19.878
	Longitude (°)		133.9317757	133.968	133.976

and secondary stress changes (e.g., Meier et al., 2014) may also be important. The evaluation of Coulomb stress change modelling depends on choices of slip models of source earthquakes, geometry of receiver faults onto which the stress tensors are projected, friction coefficients, and resolving depths. The slip distribution controls the magnitude of the Coulomb stress change, while the rupture geometry (strike, dip, rake) controls the position of positive and negative lobes. For these reasons, choosing different parameters (from different models) in calculation of ΔCFS may prompt different, even conflicting results.

The Coulomb stress change model is commonly written as (Reasenberg and Simpson, 1992; Stein, 1999; King et al., 1994):

$$\Delta CFS = \Delta\tau + \mu(\Delta\sigma_n + \Delta P) \tag{1}$$

where Δτ is the shear stress change along slip on the fault, Δσ_n is the normal stress change on the fault, ΔP is the pore pressure changes and μ is the friction coefficient. The pore pressure changes ΔP is usually proportional to the volumetric stress changes under undrained conditions, as shown by Eq. (2).

$$\Delta P = -B \frac{\Delta\sigma_{kk}}{3} \tag{2}$$

where B is the Skempton coefficient (Skempton, 1954) with a range between 0.5 and 1 depend on the rock material (ΔP can be related to confining stress in the rock by Skempton's coefficient). Δσ_{kk} is the value of normal stress. In the isotropic case, Δσ₁₁ = Δσ₂₂ = Δσ₃₃ and Δσ_{kk}/3 = Δσ (average stress) (Harris, 1998; Cocco and Rice, 2002), thus

$$\Delta P = B\Delta\sigma_n \tag{3}$$

which B is the Skempton coefficient that varies between 0 and 1.

Table 2
Four modelled scenarios for ΔCSC analyse (KF is Kunayungku scarp, WLS is western lake surprise scarp and ELS is eastern lake surprise scarp).

Feature/sequence	Sequence model #1	Sequence model #2	Sequence model #3	Sequence model #4
Kinematics source	Choy and Bowman (1990)	McCaffrey (1989)	Leonard et al. (2002)	Bowman (1991)
Hypocentral locations	Bowman and Dewey (1991)	McCaffrey (1989)	Geoscience Australia	Bowman and Dewey (1991)
Fault geometry	Calculated	Calculated	Calculated	Published
TC1	KF scarp	There is ambiguity between KF and WLS	KF	KF
TC2	TC2 split between 2 faults	No surface ruptures?	WLS	WLS
TC3	ELS	ELS	ELS	ELS
LFS	USGS kinematics and Bowman and Dewey (1991)'s relocation data	USGS kinematics and Bowman and Dewey (1991)'s relocation data	USGS kinematics and Bowman and Dewey (1991)'s relocation data	USGS kinematics and Bowman and Dewey (1991)'s relocation data

Substituting Eq. (3) in Eq. (1) gives the following equation:

$$\Delta CFS = \Delta\tau + \mu' \Delta\sigma_n \tag{4}$$

where μ' = μ(1 - B). Positive (increased) values of ΔCFS on a fault increase the likelihood that it will rupture in an earthquake, whereas failure will be delayed on a fault located in an area of negative ΔCFS.

4. Method and assumptions

To address a source of epistemic uncertainty in the applicability of Coulomb stress models to earthquake sequences, where source models vary significantly, we model five scenarios for ΔCFS triggering based on four different sets of fault models (described as 'sequence models') which primarily reflect variable interpretations of hypocentre and kinematics. The models are variably derived from (1) P wave polarity fault plane solutions, (2) teleseismic centroid body wave inversions, (3) teleseismic broadband time domain analysis, (4) detailed field investigations, surveying, and seismicity data, and (5) geometric modification of source faults in (4) to improve the fit to hypocentre locations.

Three of four sequence models (Choy and Bowman, 1990; McCaffrey, 1989; Leonard et al., 2002) have been constructed based on Leonard's (2014) scaling relationship for intraplate faults. The seismic moment magnitude from each reference is used to calculate the area of fault rupture based on the empirical relation:

$$\text{LOG}M_0 = a + b\text{LOG}(A) \tag{5}$$

where a = 6.38 and b = 1.5 (Leonard, 2014). Models (1) to (3) use calculated rupture areas to create square-shaped fault rupture planes

Table 3
The fault parameters for each sequence model.

USGS source mechanism for the Largest event before Tennant Creek main shocks (LFS)											
ID	Mb	Ms	Seismic moment (N/m)	Strike	Dip	Rake	Area (km ²)	Length (km)	Width (km)	Slip (m)	Mw
LFS (SW nodal Plane)	5.2		1.61E+17	125	32	41	16.52	4.06	4.06	0.30	5.4
LFS (NE nodal Plane)	5.2		1.61E+17	359	70	115	16.52	4.06	4.06	0.30	5.4
Sequence model #1 - Choy and Bowman (1990)											
TC1	6.1	6.3	2.9E+18	100	35	90	113.48	10.65	10.65	0.77	6.25
TC2 Fault1	6.1	6.4	4.04E+18	290	70	120	141.66	11.90	11.90	0.87	6.34
TC2 Fault2	6.1	6.4	1.15E+18	255	50	115	61.45	7.84	7.84	0.57	5.98
TC3	6.5	6.7	8.3E+18	100	45	80	228.76	15.12	15.12	1.10	6.55
Sequence model #2 - McCaffrey (1989)											
TC1 with S Nodal plane 1			3.66E+18	128	45	120	132.53	11.51	11.51	0.84	6.32
TC1 with N Nodal plane 1			3.66E+18	268	52	63	132.53	11.51	11.51	0.84	6.32
TC2			5.77E+18	117	30	100	179.52	13.40	13.40	0.97	6.45
TC3			9.77E+18	102	38	82	255.03	15.97	15.97	1.16	6.60
Sequence model #3 - Leonard et al. (2002)											
TC1	6.1	6.3		117	55	72	102.33	10.12	10.12		6.20
TC2	6.1	6.4		250	66	19	128.82	11.35	11.35		6.30
TC3	6.1	6.4		132	36	107	257.04	16.03	16.03		6.60
Sequence model #4 - Bowman (1991) (the value inside parenthesis are modified values for sequence model #5)											
TC1	6.1	6.3		112	45 (49)	90	100 (107.01)	10 (12.3)	10 (8.7)	1.1	
TC2	6.1	6.4		247	59 (63)	90	96	8	12	1.3	
TC3	6.5	6.7		113	40 (38)	90	240	15	16	2.5	

(i.e., $L = W$). Model (4) uses the Bowman (1991) fault model parameters for length, width, geometry, and slip. Model (5) adjusts model (4) parameters to improve the fit of the fault models to published hypocentral locations.

For models (1) to (3) we assume that all faults intersect the ground surface and that hypocentre is located at the midpoint along the length of the fault (i.e., bilateral rupture). Based on the definition $M_0 = \mu AD$, we calculate the amount of average slip for each fault and assume a uniform slip distribution. References and details for fault models (1) to (4) are presented in Table 2, models (1) to (5) parameters are summarized in Table 3, and a representative map view of the faults for models (1) to (4) is presented in Fig. 2.

We compute the stress changes using the Coulomb 3.3 software (Toda et al., 2011) which calculates the static stress changes resulting from fault rupture in an elastic half-space, following the theoretical approach of Okada (1992). A value of $\mu' = 0.4$ is used in the calculations, which is generally employed to minimize the uncertainty in the apparent friction coefficient (e.g., King et al., 1994; Avouac et al., 2014; Green et al., 2015). Each of the four model faults are discretised into patches ~ 1 km along strike and ~ 1 km in depth.

5. Results

5.1. Defining the fault model for the largest foreshock

For the largest recorded foreshock (LFS), we use the slip kinematics and seismic moment magnitude from the USGS database (<https://earthquake.usgs.gov/earthquakes/eventpage/usp00031hu/executive>) and assume that Bowman and Dewey's (1991) relocated hypocentre occurs in the centre of the fault. As we do not know which fault plane (nodal vs. auxiliary) is the actual fault plane, we construct two fault models using Leonard's (2014) scaling relation and consider both fault orientations in each scenario. Using M_0 as 1.61×10^{24} dyn cm, which is taken from USGS, we find the fault area as 16.51 km^2 (Table 3). The evaluated length and width of the LFS fault are 4.06 km and amount of average slip for this fault is 0.29 m (Table 3).

5.2. Coulomb stress change calculations

The results below explain the ΔCFS changes calculated for each of the five fault models that we investigated (Figs. 3–7). For each model, the top panel shows a transparent plan view of fault geometry,

including all intersections. The fault colors follow the convention established in Fig. 2. The Lower panel (A–...) shows accumulated ΔCFS maps for progressively later rupturing faults (downwards). Left and right maps show accumulated ΔCFS for east and southwest-dipping LFS nodal planes, respectively. The intersections of the planar, rectangular faults are shown on the top panel and dashed lines on individual ΔCFS maps. Although the faults are modelled as rectangular and extensively intersecting at depth, they do not intersect that way at the surface and it is likely that the true configuration consists of faults that terminate against each other.

Each sequence begins with either an east-dipping or southwest-dipping nodal plane for the LFS (derived in 5.1 above). For sequence model 2 (Section 5.2.2) we also show a separate progression using an alternative fault model for the TC1 mainshock.

5.2.1. Sequence model 1 – Choy and Bowman (1990)

In this model, we take the fault location from Bowman and Dewey (1991) and the fault plane solutions from Choy and Bowman (1990) (Table 2) who used teleseismic data to determine source mechanisms and hypothesized that three subevents for each main shock represent the best-fit solution to constrain fault orientations. The fault plane orientation of the three subevents of TC1 and TC3 are the same and we build continuous straight faults for TC1 and TC3. However, the third sub-event of TC2 differs in orientation to the first two; the moment ratios are 1.0, 3.2 and 1.2 respectively (Choy and Bowman, 1990). We therefore construct two fault models for TC2; one has the orientation of the two first subevents (TC2a) and their allocation of moment magnitude, the other (TC2b) has the orientation and moment magnitude allocation of the 3rd subevent (Table 3).

The Coulomb stress changes for this sequence are shown in Fig. 3 where the pictures on the left (A, C and E) are based on the assumption that the LFS fault plane dips east and those on the right (B, D and F) assume a SW dipping fault plane. Regardless of this choice, the stress changes on TC1 are similar, with positive ΔCFS on 81% (E) (Fig. 3A) or 78% (SW) (Fig. 3B) of the fault rupture plane. The largest ΔCFS within 2 km of the hypocentre of TC1 is 2.35 bars (E) or 2.01 bars (SW). ΔCFS values are provided in Table 4 and probability density functions and stress distributions of all the stress changes can be found in the Appendix 1.

The amalgamation of LFS plus TC1 generates positive ΔCFS of 34.72% (E) (Fig. 3C) or 36.11% (SW) (Fig. 3D) on the TC2a fault rupture plane. The largest ΔCFS within 2 km of the hypocentre of TC2a

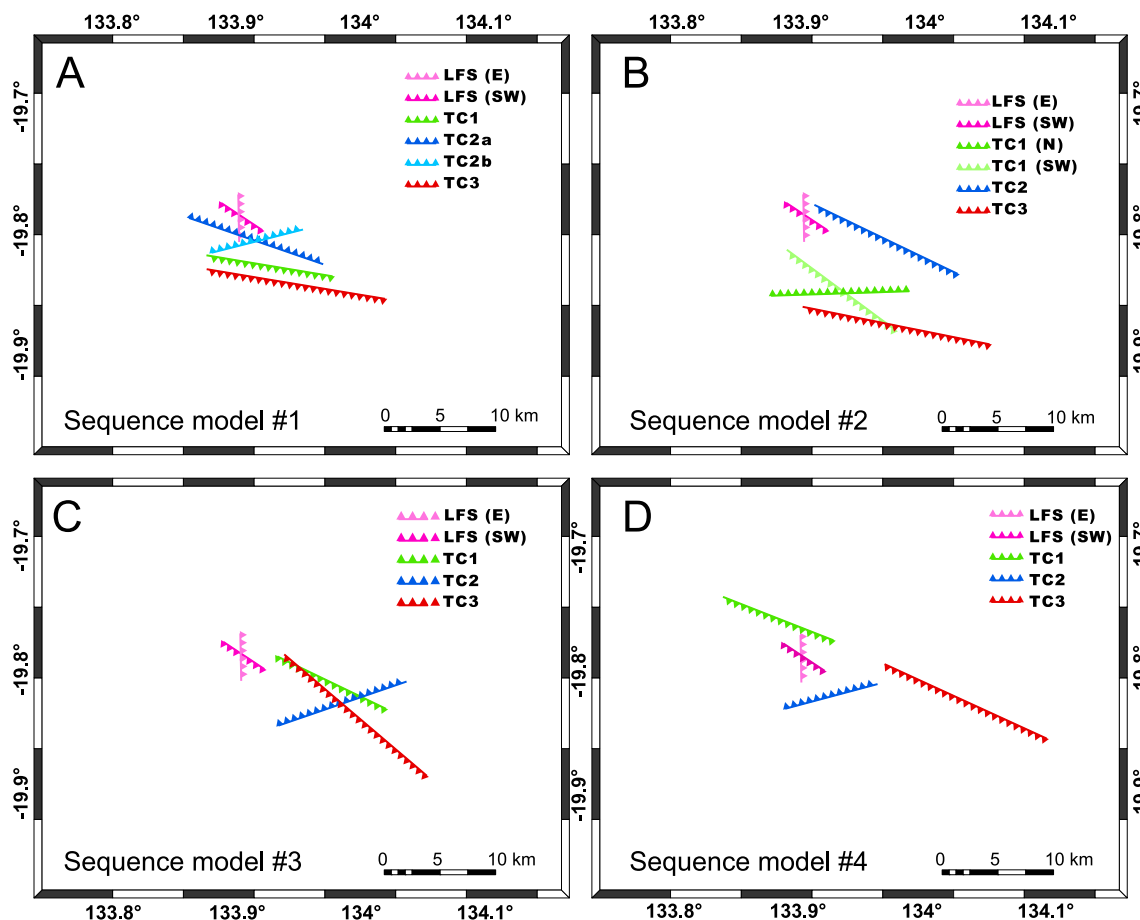


Fig. 2. A schematic view of the location and orientation of the faults for each sequence (purple ones for LFS, green ones for TC1, blue ones for TC2 and red ones for TC3). (For interpretation of the references to color in this figure legend, the reader is referred to the web version of this article.)

is 1.17 bars (E) or 3.74 bars (SW). Earthquakes LFS + TC1 + TC2a generate positive Δ CFS on 12.5% (E) (Fig. 3E) or 10.94% (SW) (Fig. 3F) of the TC2b fault rupture. The maximum Δ CFS within 2 km of the hypocentre of TC2b is negative (-1.35 bars) (E) or -4.76 bars (SW) from LFS with SW nodal plane, TC1, and TC2a.

Earthquakes LFS + TC1 + TC2a + TC2b generate positive Δ CFS on 38.22% of TC3 (both) (Fig. 3G, H) and the maximum value within 2 km of the TC3 hypocentre is 19.71 bars (E) or 19.74 bars (SW).

5.2.2. Sequence model 2 – McCaffrey (1989)

McCaffrey (1989) relocated main shocks using teleseismic long period P and SH and short period P waves and produced a three-fault model for the 1988 sequence which we use here. However, McCaffrey (1989) argue that TC1 is the only one of three events that display a nodal plane consistent with a north dip on WLS fault. We therefore consider two possible faults for TC1; one dipping S, the other dipping N (Table 3). The Coulomb stress changes for this sequence are shown in Fig. 4 where the pictures on the left (A, C, E and G) are based on the assumption that the LFS fault plane dips east and those on the right (B, D, F and H) assume a SW dipping fault plane.

LFS produces positive stress changes on 62.81% (E-dipping LFS) (Fig. 4A) and 61.15% (SW-dipping LFS) (Fig. 4B) on TC1 (S-dipping). The largest Δ CFS within 2 km of the TC1 (S) hypocentre is 0.50 bars (LFS E) or 0.36 bars (LFS SW). LFS produces positive stress changes on 79.34% (E) (Fig. 4C) or 80.17% (SW) on the N-dipping TC1 fault (Fig. 4D). The largest Δ CFS within 2 km of the TC1 (N) hypocentre is 0.52 bars (E) and 0.54 bars (SW).

The culmination of LFS (either E or SW) plus TC1 (S) generates positive Δ CFS on 10.06% (Fig. 4E and F) of TC2. The largest Δ CFS

within 2 km of TC2 hypocentre is -0.72 bars (E) or -0.62 (SW). LFS plus TC1 (N) generates positive Δ CFS on 14.29% (E) (Fig. 4G) or 14.79% (SW) (Fig. 4H) of TC2. The largest Δ CFS within 2 km of the TC2 hypocentre is -0.81 bars (E) or -0.74 (SW). Earthquakes LFS (E or SW) + TC1 (S) + TC2 generate positive Δ CFS on 49.61% (Fig. 4I and J) of TC3; the maximum Δ CFS within 2 km of the hypocentre is 21.07 bars. Earthquakes LFS (E or SW) + TC1 (N) + TC2 generate positive Δ CFS on 39.84% (Fig. 4K and L) of TC3 fault (Table 5). The maximum Δ CFS within 2 km is 4.41 bars. As can be seen from Fig. 4I, J, K and L, the stress pattern on TC3 is different depending on the choice of the fault plane for TC1.

5.2.3. Sequence model 3 - Leonard et al. (2002)

Leonard et al. (2002) compiled data and produced p wave first motion focal mechanisms, with preferred fault planes based on field observations from Jones et al. (1991) and hypocentres from Australian Geoscience Seismological Centre (AG) (Table 3).

The Coulomb stress changes for this sequence are shown in Fig. 5, where the pictures on the left (A, C and E) are based on the assumption that the LFS fault plane dips east and those on the right (B, D and F) assume a SW dipping fault plane. Regardless of this choice, the stress changes on TC1 are similar, with positive Δ CFS on 100% (E) (Fig. 5A) or 98% (SW) (Fig. 5B) of the fault rupture plane. The largest Δ CFS within 2 km of the hypocentre of TC1 is 0.39 bars (E) or 0.58 bars (SW) (Table 6). Earthquakes LFS + TC1 generate positive Δ CFS on 28.93% (Fig. 5C) (E) or 28.10% (Fig. 5D) (SW) of the TC2 fault rupture plane; the largest Δ CFS within 2 km of the hypocentre of TC2 is 1.19 bars (E) or 1.27 bars (SW) from LFS with SW nodal plane and TC1. Earthquakes LFS + TC1 + TC2 generate positive Δ CFS on 50% (E) (Fig. 5E) and

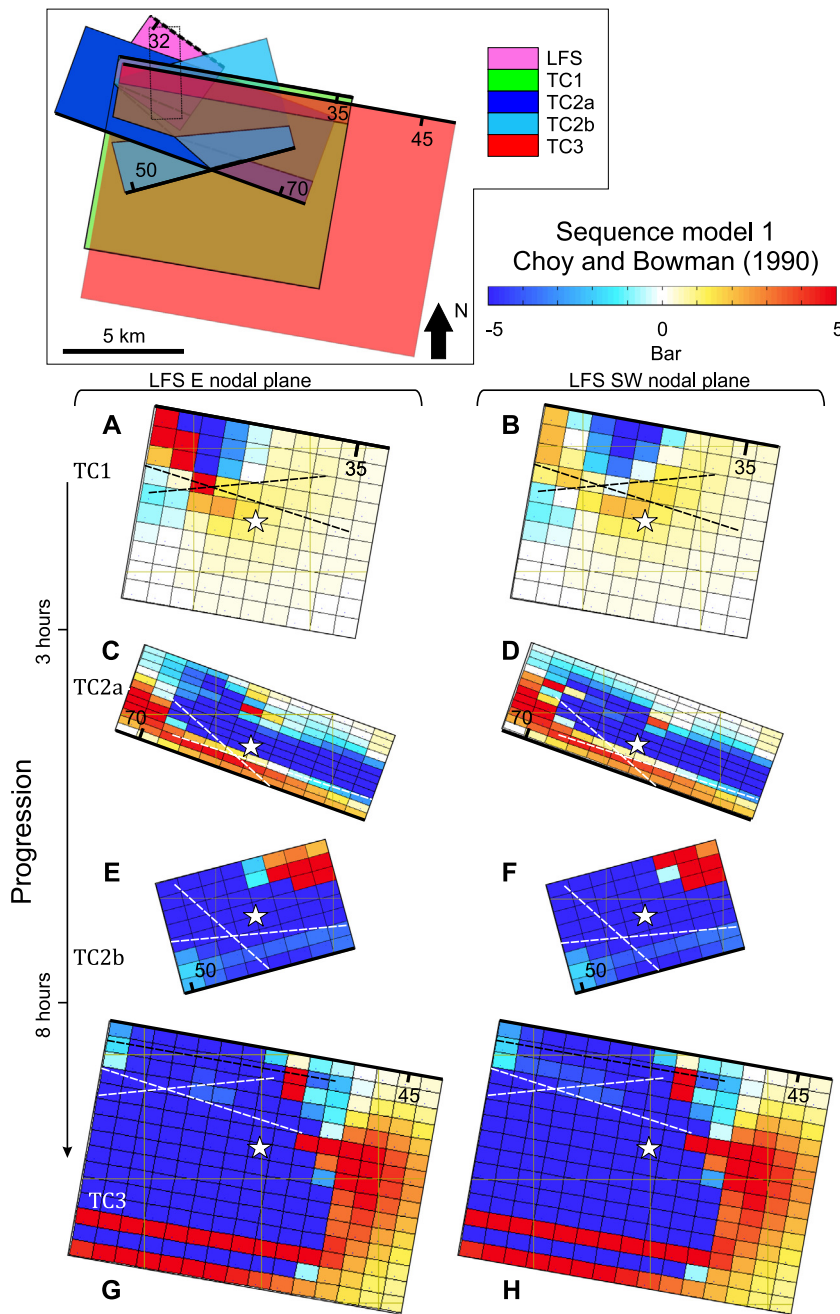


Fig. 3. Cumulative coseismic Δ CFS (sequence model #1) Top panel - transparent plan view of fault geometry, including intersections. For fault colors see Fig. 2. Lower panel - cumulative Δ CFS maps for progressively later rupturing faults (downwards) and east or southwest-dipping LFS nodal planes (left and right, respectively). All dashed lines indicate fault intersections and white stars are hypocentres. (A) LFS with E nodal plane on TC1 (B) LFS with SW nodal plane on TC1 (C) LFS with E nodal plane + TC1 on TC2a (D) LFS with SW nodal plane + TC1 on TC2a (E) LFS with E nodal plane + TC1 + TC2a on TC2b (F) LFS with SW nodal plane + TC1 + TC2a on TC2b (G) LFS with E nodal plane + TC1 + TC2a + TC2b on TC3 and (H) LFS with SW nodal plane + TC1 + TC2a + TC2b on TC3.** (Probability density function graphs (PDF) (i) and depth distribution graphs (ii) of Cumulative coseismic Δ CFS for each figure in this sequence model are shown in Fig. 1 in Appendix 1.)**

49.61% (SW) (Fig. 5F) of TC3 and the maximum value within 2 km of the TC3 hypocentre is -5.09 bars (E) or -7.67 bars (SW).

5.2.4. Sequence model 4 – Bowman (1991)

Bowman (1991) modelled Tennant Creek main shock faults based on detailed field investigations, surveying, and mainshock and after-shock data, and published detailed fault parameters including strike, dip, length, width and average slip during faulting (Table 3). He constrained the rakes to be 90° as reverse faulting was the dominant style of deformation seen in the field (Bowman et al., 1990a, 1990b) and in the main-shock focal mechanisms (e.g., McCaffrey, 1989; Choy and Bowman, 1990). The relocated hypocentres from Bowman and Dewey (1991) were used in the study of Bowman (1991).

The Coulomb stress changes for this sequence are shown in Fig. 6 where the pictures on the left (A, C and E) assume that the LFS fault plane dips east and those on the right (B, D and F) assume a SW dipping

fault plane. Regardless of this choice, the stress changes on TC1 are similar, with positive Δ CFS on 43% (E-dipping LFS) (Fig. 6A) or 53% (SW-dipping LFS) (Fig. 6B) of the TC1's fault rupture plane. However, the relocated hypocentre for TC1 from Bowman and Dewey (1991) does not intersect with the published fault plane from Bowman (1991). Bowman (1991) argue that although the relocated epicentres of the first two main shocks nucleated nearby, they do not help connect the main shocks with fault segments. However, arrival time data from Warrawunga array alone suggest that TC2 lay east of TC1 (Bowman, 1988), and evidence from the rupture directivity and focal mechanisms imply that MS2 ruptured the more complicated central section (WLS). If we assume that TC1 ruptured the deeper part of the TC1 fault at a depth of 6.5 km (relocated depth from Bowman and Dewey, 1991), earthquakes LFS plus TC1 generate positive Δ CFS on 48.96% (E) (Fig. 6C) or 46.88% (SW) (Fig. 6D) of the TC2 fault rupture plane. Moreover, if we assume the TC2 ruptured at depth 3.5 km, earthquakes LFS

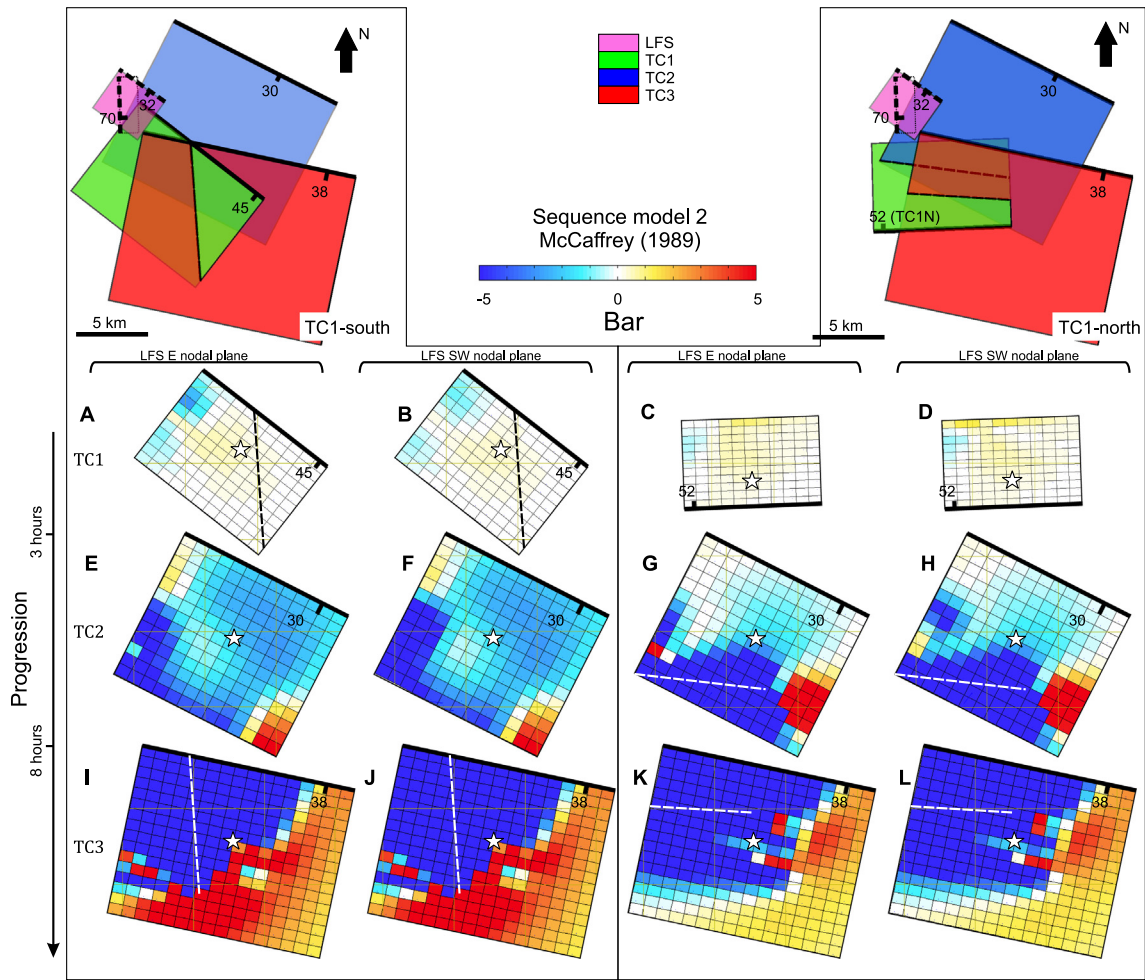


Fig. 4. Cumulative coseismic ΔCFS (sequence model #2) Top panel - transparent plan view of fault geometry, including intersections. For fault colors see Fig. 2. Lower panel - cumulative ΔCFS maps for progressively later rupturing faults (downwards) and east or southwest-dipping LFS nodal planes (left and right, respectively). All dashed lines indicate fault intersections and white stars are hypocentres. (A) LFS with E nodal plane on TC1 with S nodal plane (B) LFS with SW nodal plane on TC1 with S nodal plane (C) LFS with E nodal plane on TC1 with N nodal plane (D) LFS with SW nodal plane on TC1 with N nodal plane (E) LFS with E nodal plane + TC1 with S nodal plane on TC2 (F) LFS with SW nodal plane + TC1 with S nodal plane on TC2 (G) LFS with E nodal plane + TC1 with N nodal plane on TC2 (H) LFS with SW nodal plane + TC1 with N nodal plane on TC2 (I) LFS with E nodal plane + TC1 with S nodal plane + TC2 on TC3 (J) LFS with SW nodal plane + TC1 with S nodal plane + TC2 on TC3 (K) LFS with E nodal plane + TC1 with N nodal plane + TC2 on TC3 and (L) LFS with SW nodal plane + TC1 with N nodal plane + TC2 on TC3.** (Probability density function graphs (PDF) (i) and depth distribution graphs (ii) of Cumulative coseismic ΔCFS for each figure in this sequence model are shown in Fig. 2 in Appendix 1.)**

(both) + TC1 + TC2 generate positive ΔCFS on 98.33% of TC3 (Fig. 6E and F) (Table 7).

5.2.5. Sequence model 5 – modified from Bowman (1991) (sequence model#4)

This sequence model is generally equivalent to sequence model 4 but uses a fault model that we have modified by altering the TC1 fault plane to intersect the TC1 hypocentre. This required small changes in the dip (increase 45–49), length (increase 10 to 12.3 km) and width (decrease 10–8.7 km), resulting in an increase of the TC1 fault area from 100 km² to 107.01 km². These changes are within the error of the original model. For consistency, we modified the other faults slightly to coincide with their earthquake hypocentres. Moreover, since the relocated TC2 hypocentre from Bowman and Dewey (1991) inside the TC2's fault, we just need modify the dip from 59 to 63, moreover, for TC3, we need to decrease the dip from 40 to 38. The modified values for each fault are shown in the parenthesis in Table 3.

The Coulomb stress changes for this sequence are shown in Fig. 7 where the pictures on the left (A, C and E) assume that the LFS fault plane dips east and those on the right (B, D and F) assume a SW dipping

fault plane. Regardless of this choice, the stress changes on TC1 are almost similar, with positive ΔCFS on 40% (E) (Fig. 7A) or 44% (SW) (Fig. 7B) of the fault rupture plane. The largest ΔCFS within 2 km of the TC1 (S) hypocentre is 0.72 bars (E) or 1.02 bars (SW). Earthquakes LFS plus TC1 generate positive ΔCFS on 41% (E) (Fig. 7C) or 35% (SW) (Fig. 7D) of the TC2 fault rupture plane; the largest ΔCFS within 2 km of the hypocentre of TC2 is 13.51 bars (E) or 12.6 bars (SW) from LFS with SW nodal plane and TC1. Moreover, earthquakes LFS (both) + TC1 + TC2 generate positive ΔCFS on 99.16% (Fig. 7E and F) of TC3 and the maximum value within 2 km of the TC3 hypocentre is 5.94 bars (E) or 5.9 bars (SW) (Table 8).

In the absence of better data, we have used the uniform slip distribution to model slip across the fault plane, but faults are unlikely to display entirely uniform slip distributions. Many slip distributions can be approximated by a bulls-eye pattern (e.g., Beavan et al., 2012), so we additionally used the most refined and data-integrative model (Sequence Model 5) as a case study to test the relative validity of a uniform-average versus a bulls-eye pattern of slip distribution.

The TC1 mainshock hypocentre was located in the SE corner of the fault, which led Bowman (1991) to suggest that TC1 ruptured from SE

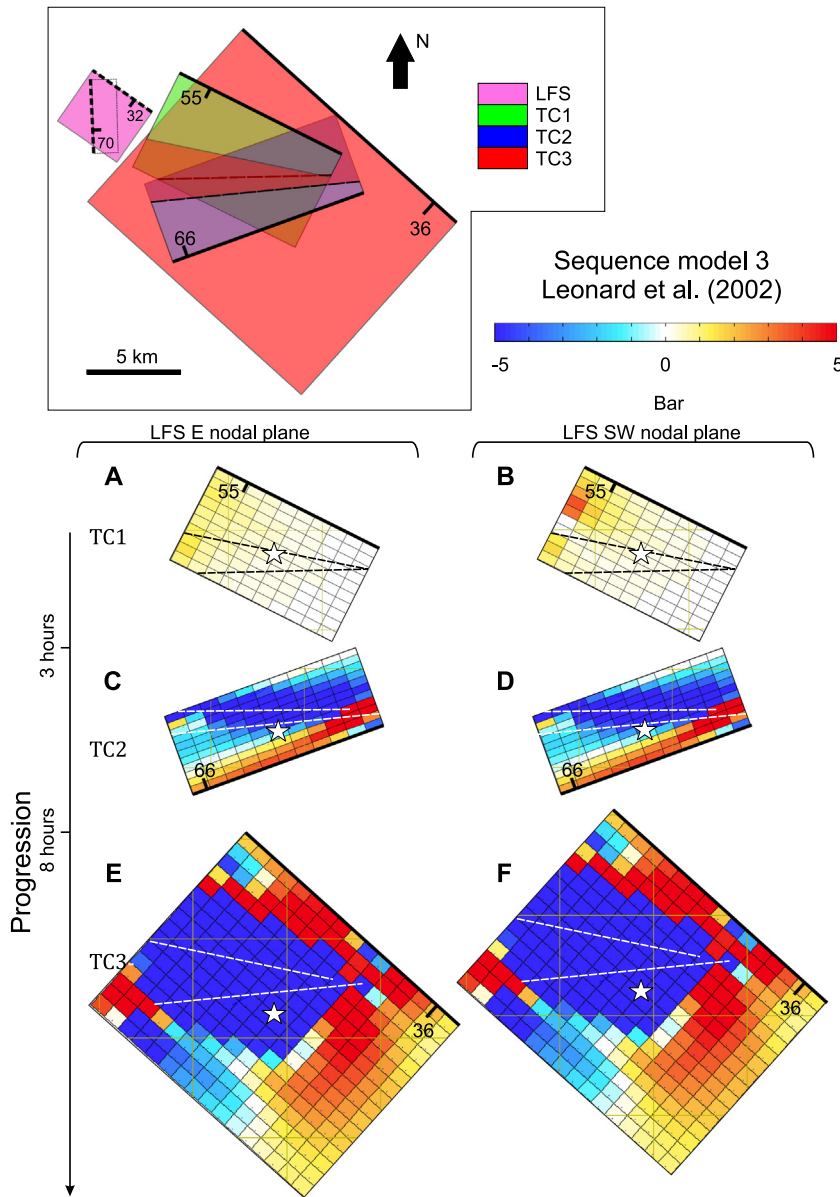


Fig. 5. Cumulative coseismic ΔCFS (sequence model #3) Top panel - transparent plan view of fault geometry, including intersections. For fault colors see Fig. 2. Lower panel - cumulative ΔCFS maps for progressively later rupturing faults (downwards) and east or southwest-dipping LFS nodal planes (left and right, respectively). All dashed lines indicate fault intersections and white stars are hypocentres. (A) LFS with E nodal plane on TC1 (B) LFS with SW nodal plane on TC1 (C) LFS with E nodal plane + TC1 on TC2 (D) LFS with SW nodal plane + TC1 on TC2 (E) LFS with E nodal plane + TC1 + TC2 on TC3 (F) LFS with SW nodal plane + TC1 + TC2 on TC3.** (Probability density function graphs (PDF) (i) and depth distribution graphs (ii) of Cumulative coseismic ΔCFS for each figure in this sequence model are shown in Fig. 3 in Appendix 1.)**

to NW. Several studies have shown that faults that rupture unilaterally display an offset between the locations of the hypocentre and centroid (see for example the locations of hypocentre versus centroid on the Charing Cross Fault in the Canterbury Earthquake Sequence; Beavan et al., 2012), so we adopt a bulls-eye pattern for slip distribution on TC1, with the centroid centred on the fault and remote from the hypocentre. TC2 ruptured bilaterally from about 3.5 km depth, so we centre the bullseye on that depth.

For each fault, we ensure that the slip at the corners of the fault decline to near zero. We further ensure that the average slip for the entire fault is consistent with the literature values of average slip from Bowman (1991) for Tennant Creek main shocks and with the scaled average slip of 0.29 m for the LFS derived from fault dimension scaling relationships of Leonard (2014). We derive maximum slip values from the ratio of average to maximum slip reported by Wesnousky (2008). The maximum slip calculated at centre of each fault are 0.82 m for LFS (with average slip of 0.29), for TC1 is 3.14 m (with average slip of 1.1 m) and for TC2 is 3.71 m (with average slip of 1.3 m).

The Coulomb stress changes for the sequence model #5 with bulls-eye slip distribution are shown in Fig. 7(G–L), where the pictures 7 G, I and K, assume that the LFS fault plane dips east and the pictures 7 H, J

and L, assume a SW dipping fault plane. Regardless of this choice, the stress changes on TC1 are almost similar, with positive ΔCFS on 54.16% (E) (Fig. 7G) or 40.32% (SW) (Fig. 7H) of the fault rupture plane. The largest ΔCFS within 2 km of the TC1 (S) hypocentre is 1.02 bars (E) or 1.27 bars (SW). Earthquakes LFS plus TC1 generate positive ΔCFS on 40.62% (E) (Fig. 7I) or 39.58% (SW) (Fig. 7J) of the TC2 fault rupture plane; the largest ΔCFS within 2 km of the hypocentre of TC2 is 82.83 bars (E) or 82.54 bars (SW) from LFS with SW nodal plane and TC1. Moreover, earthquakes LFS (both) + TC1 + TC2 generate positive ΔCFS on 100% (Fig. 7K and L) of TC3 and the maximum value within 2 km of the TC3 hypocentre is 1.44 bars (Table 8).

6. Discussion

6.1. Coulomb triggering and the Tennant Creek sequence

We explored the possible stress triggering relationship of the Tennant Creek earthquakes with different fault source (sequence) models. We do not account for other sources of stress such as dynamic or visco-elastic stress changes (Van Der Elst and Brodsky, 2010; Kilb et al., 2000; Felzer and Brodsky, 2005, 2006) or secondary aftershock

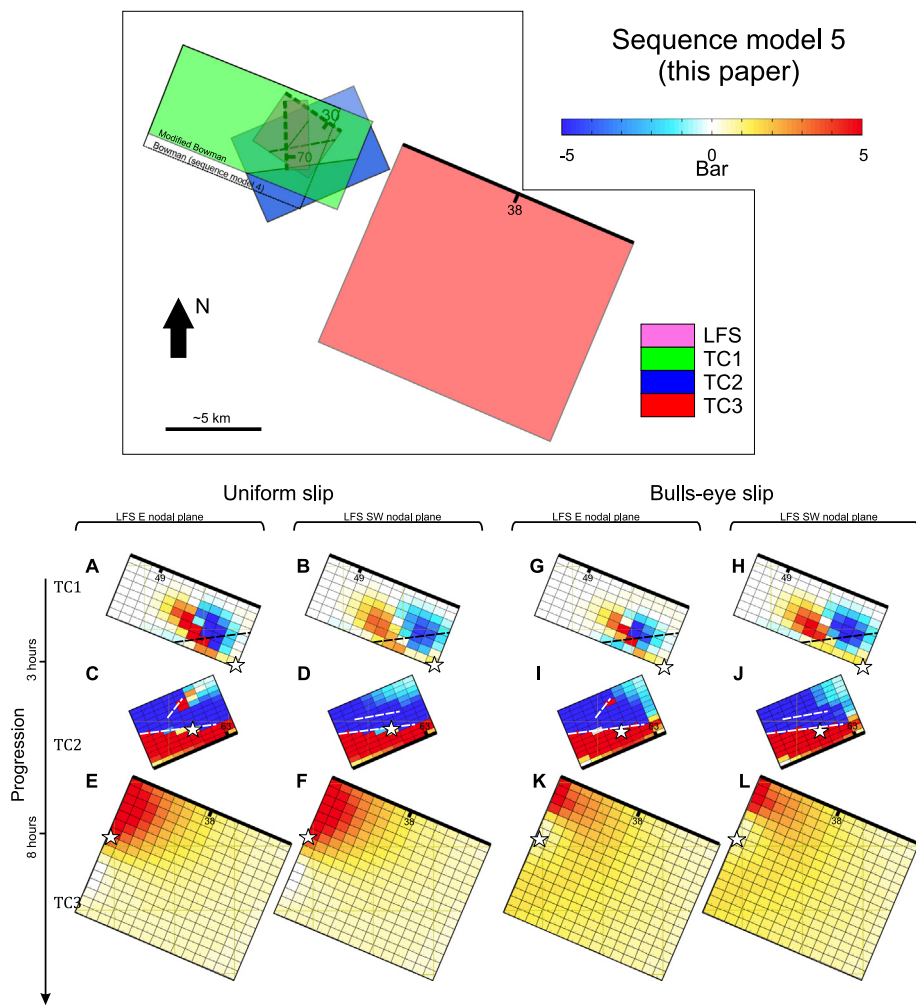


Fig. 7. Cumulative coseismic ΔCFS (sequence model #5) with uniform slip (A–F) and bulls-eye slip (G–L) distribution. Top panel - transparent plan view of fault geometry, including intersections. For fault colors see Fig. 2. Lower panel - cumulative ΔCFS maps for progressively later rupturing faults (downwards) and east or southwest-dipping LFS nodal planes (left and right, respectively). All dashed lines indicate fault intersections and white star are hypocentres. (A and G) LFS with E nodal plane on TC1 (B and H) LFS with SW nodal plane on TC1 (C and I) LFS with E nodal plane + TC1 on TC2 (D AND J) LFS with SW nodal plane + TC1 on TC2 (E and K) LFS with E nodal plane + TC1 + TC2 on TC3 (F and L) LFS with SW nodal plane + TC1 + TC2 on TC3.** (Probability density function graphs (PDF) (i) and depth distribution graphs (ii) of Cumulative coseismic ΔCFS for each figure in this sequence model are shown in Fig. 5 (for uniform slip distribution) and Fig. 6 (for bulls-eye slip distribution) in Appendix 1.)**

ΔCFS from its preceding events.

If the ΔCFS within 2 km of receiver fault hypocentres is considered, the (most-refined and data-integrative) model 5 sequence (TC1,2,3) is entirely consistent with earthquake-triggering by Coulomb stress change (i.e., all events on receiver faults initiated where ΔCFS exceeded positive ‘threshold’ values for earthquake triggering from comparative studies; Fig. 8) (Stein et al., 1994; King and Cocco, 2001; Reasenberg and Simpson, 1992). Model 1 is almost entirely consistent with ΔCFS -induced triggering (all events except TC2b), and models 2 and 3 contain only some events that are consistent with ΔCFS -induced triggering (Model 2 = TC1,3; Model 3 = TC1,2). Model 4 does not have hypocentres that co-locate to their source fault planes. Collectively, this suggests that different input data (that inform the models) and different source modelling approaches can yield source models with enough variability (manifested as epistemic uncertainty) that the role of static stress changes in the spatiotemporal evolution of the earthquake sequence is not immediately clear (and possibly discrepant for different models). With progressive knowledge increase, the refinement of source models may enable better evaluation of the role of static stress transfer. In this case, we demonstrate that the ‘most informed fault model’ also yields ΔCFS model results that are most consistent with earthquake-triggering by static stress changes at impending hypocentres of receiver faults. Notably, all faults in all models have some regions where ΔCFS changes were positive; this introduces some ambiguity in the interpretations of stress-triggering given the epistemic uncertainties in hypocentral location (perhaps some hypocentres in models 2 and 3 are sufficiently mis-located such that they actually reside in positive ΔCFS domains?).

The processes by which one earthquake may trigger another are complex and influenced by additional factors such as dynamic triggering, heterogeneous pre-sequence stress conditions (Mildon et al., 2017; Wedmore et al., 2017; Verdecchia et al., 2018; Mildon et al., 2018) and variations in fault friction and fluid pressures (e.g. Wang et al., 2014; King and Devès, 2015). These factors add additional uncertainty in evaluating the relationships between ΔCFS variations and earthquake nucleation sites. Using Coulomb stress modelling results, Mildon et al. (2016) state that fault location is more important than fault orientation on the effects of stress interactions. However, structural complexity in fault networks (including gaps, bends, stepovers and intersections between faults) sometimes appears to halt rupture propagation during earthquakes and sometimes permits through-going rupture, allowing large multi-segment earth-quakes (e.g. Biasi and Wesnousky, 2016). Scholz (2010) hypothesized that faults that are proximal in space and have similar slip rates can become synchronized, such that they tend to rupture concurrently. The main reason for such mechanism might be static stress increases related with a ruptured fault bring adjacent faults closer to the end of their earthquake cycle, and during time the cycles on various faults turn out to be temporally aligned. It is possible that the faults responsible for the Tennant Creek earthquake sequence exhibit similar behaviour.

6.2. Time variation intervals versus ΔCFS

To evaluate the possible relationship between ΔCFS magnitudes and the time interval between ΔCFS -triggered events in the Tennant Creek earthquake sequence, we compile the time interval between source and

Table 4
Coseismic Coulomb stress changes induced by preceding events on the fault rupture of each subsequent event for sequence model #1.

Receiver Faults→	TC1		TC2 (a)		TC2 (b)		TC3	
	Largest ΔCFS around hypo (bar)	≥ 0.1 (%)	≥ 0.01 (%)	≥ 0 (%)	Largest ΔCFS around hypo (bar)	≥ 0.1 (%)	≥ 0.01 (%)	≥ 0 (%)
LFS (SW)	2.01	59.00	78.00	78.00				
LFS (E)	2.35	63.00	80.00	81.00				
LFS (SW) + TC1			3.74	36.11				
LFS (E) + TC1			1.17	34.72				
LFS (SW) + TC1 + TC2 (#1)					-4.76	10.94	10.94	10.94
LFS (E) + TC1 + TC2 (#1)					-1.35	12.50	12.50	12.50
LFS (SW) + TC1 + TC2 (#1) + TC2 (#2)								19.74
LFS (E) + TC1 + TC2 (#1) + TC2 (#2)								19.71
								38.22
								38.22

Table 5
Coseismic Coulomb stress changes induced by preceding events on the fault rupture of each subsequent event for sequence model #2.

Receiver faults→	TC1 (S nodal plane)		TC1 (N nodal plane)		TC 2		TC 3	
	Largest ΔCFS around hypo (bar)	≥ 0.1 (%)	≥ 0.01 (%)	≥ 0 (%)	Largest ΔCFS around hypo (bar)	≥ 0.1 (%)	≥ 0.01 (%)	≥ 0 (%)
LFS (SW)	0.36	26.45	55.37	61.16	0.52	51.24	78.51	80.17
LFS (E)	0.5	28.10	56.20	62.81	0.54	57.85	76.86	79.34
LFS (SW) + TC1 (S nodal plane)								
LFS (E) + TC1 (S nodal plane)					-0.62	9.47	10.06	10.06
LFS (SW) + TC1 (N nodal plane)					-0.72	9.47	10.06	10.06
LFS (SW) + TC1 (N nodal plane)					-0.74	13.02	14.79	14.79
LFS (E) + TC1 (N nodal plane)					-0.71	12.50	14.29	14.29
LFS (SW) + TC1 (S nodal plane) + TC2								21.7
LFS (E) + TC1 (S nodal plane) + TC2								49.61
LFS (SW) + MS1 (N nodal plane) + TC2								21.7
LFS (E) + TC1 (N nodal plane) + TC2								49.61
								4.41
								38.67
								39.84
								4.41
								38.67
								39.84

Table 6
Coseismic Coulomb stress changes induced by preceding events on the fault rupture of each subsequent event for sequence model #3.

Receiver faults→	TC1				TC2				TC3			
Source faults↓	Largest ΔCFS around hypo (bar)	≥ 0.1 (%)	≥ 0.01 (%)	≥ 0 (%)	Largest ΔCFS around hypo (bar)	≥ 0.1 (%)	≥ 0.01 (%)	≥ 0 (%)	Largest ΔCFS around hypo (bar)	≥ 0.1 (%)	≥ 0.01 (%)	≥ 0 (%)
LFS (SW)	0.58	63.00	98.00	98.00								
LFS (E)	0.39	64.00	100.00	100.00								
LFS (SW) + TC1					1.27	28.10	28.10	28.10				
LFS (E) + TC1					1.19	28.10	28.93	28.93				
LFS (SW) + TC1 + TC2									-7.67	49.61	49.61	49.61
LFS (E) + TC1 + TC2									-5.09	49.61	50.00	50.00

Table 7
Coseismic Coulomb stress changes induced by preceding events on the fault rupture of each subsequent event for sequence model #4.

Receivers faults→	TC1				TC2				TC3			
Source faults↓	Largest ΔCFS around hypo (bar)	≥ 0.1 (%)	≥ 0.01 (%)	≥ 0 (%)	Largest ΔCFS around hypo (bar)	≥ 0.1 (%)	≥ 0.01 (%)	≥ 0 (%)	Largest ΔCFS around hypo (bar)	≥ 0.1 (%)	≥ 0.01 (%)	≥ 0 (%)
LFS (SW)	-	32.00	50.00	53.00								
LFS (E)	-	26.00	41.00	43.00								
LFS (SW) + TC1					-	43.75	44.79	46.88				
LFS (E) + TC1					-	46.88	48.96	48.96				
LFS (SW) + TC1 + TC2									-	96.25	98.33	98.33
LFS (E) + TC1 + TC2									-	96.25	98.33	98.33

receiver fault ruptures versus ΔCFS changes within 2 km of the hypocentre for 53 earthquake sequences in continental regions and compare them to our results (Fig. 8A). The time interval “t” between LFS and TC1 (1 year and 13 days), TC1 and 2 (3 h), and TC 2 and 3 (8 h) is shortest for highest values of ΔCFS and increases with decreasing ΔCFS (Fig. 8A). The global data is highly scattered, with no clear relationship between “t” and ΔCFS. This may reflect large variations resulting from different modelling approaches, different tectonic settings, different stress states, and other variations. However, we note that the TC1-2 and TC2-3 values for “t” and ΔCFS are amongst the shortest and largest, respectively, in the investigated dataset. The average “t” for these 53 earthquake sequences is 3880 days; this indicates that static stress changes have been previously hypothesized to explain earthquake triggering for “t” ≈ 10 years up to 108 years. Most of the earthquakes investigated (about 70%) occurred with “t” ≤ 10 years and ΔCFS ≥ 0.1bars. (The data represented here are shown in Appendix 2.)

In Fig. 8B, we plot the cumulative (coseismic, postseismic and interseismic) ΔCFS accumulated at receiver fault hypocentre locations immediately prior to the forthcoming earthquake. This data was obtained for 30 earthquake sequences and compared to the Tennant Creek events. The ΔCFS values for TC 2 and TC 3 are higher than average and median values but consistent with some other events (events #17, 18, 19 and 21). TC1 is slightly below the median and well below the average. Collectively, we propose that the median ΔCFS (1 bar) and average ΔCFS (3.71 bar) values derived herein provide a useful context with which to evaluate possible roles of static stress in earthquake-triggering. The range of published values (0.05 bar to > 20 bar) highlight the variability in these data and the challenge in applying the concept of a ΔCFS earthquake-triggering ‘threshold’ more universally.

Table 8
Coseismic Coulomb stress changes induced by preceding events on the fault rupture of each subsequent event for sequence model #5 with uniform slip distribution and bulls-eye slip distribution.

Receivers faults→	TC1				TC2				TC3			
Source faults↓	Largest ΔCFS around hypo (bar)	≥ 0.1 (%)	≥ 0.01 (%)	≥ 0 (%)	Largest ΔCFS around hypo (bar)	≥ 0.1 (%)	≥ 0.01 (%)	≥ 0 (%)	Largest ΔCFS around hypo (bar)	≥ 0.1 (%)	≥ 0.01 (%)	≥ 0 (%)
Uniform slip distribution												
LFS (SW)	1.02	33	43	44								
LFS (E)	0.72	29	37	40								
LFS (SW) + TC1					12.6	35	35	35				
LFS (E) + TC1					13.51	41	41	41				
LFS (SW) + TC1 + TC2									5.9	98.75	99.16	99.16
LFS (E) + TC1 + TC2									5.94	98.75	99.16	99.16
Bulls-eye slip distribution												
LFS (SW)	1.27	28.8	39.36	40.32								
LFS (E)	1.02	29.16	47.91	54.16								
LFS (SW) + TC1					82.54	39.58	39.58	39.58				
LFS (E) + TC1					82.83	40.62	40.62	40.62				
LFS (SW) + TC1 + TC2									1.44	100	100	100
LFS (E) + TC1 + TC2									1.44	100	100	100

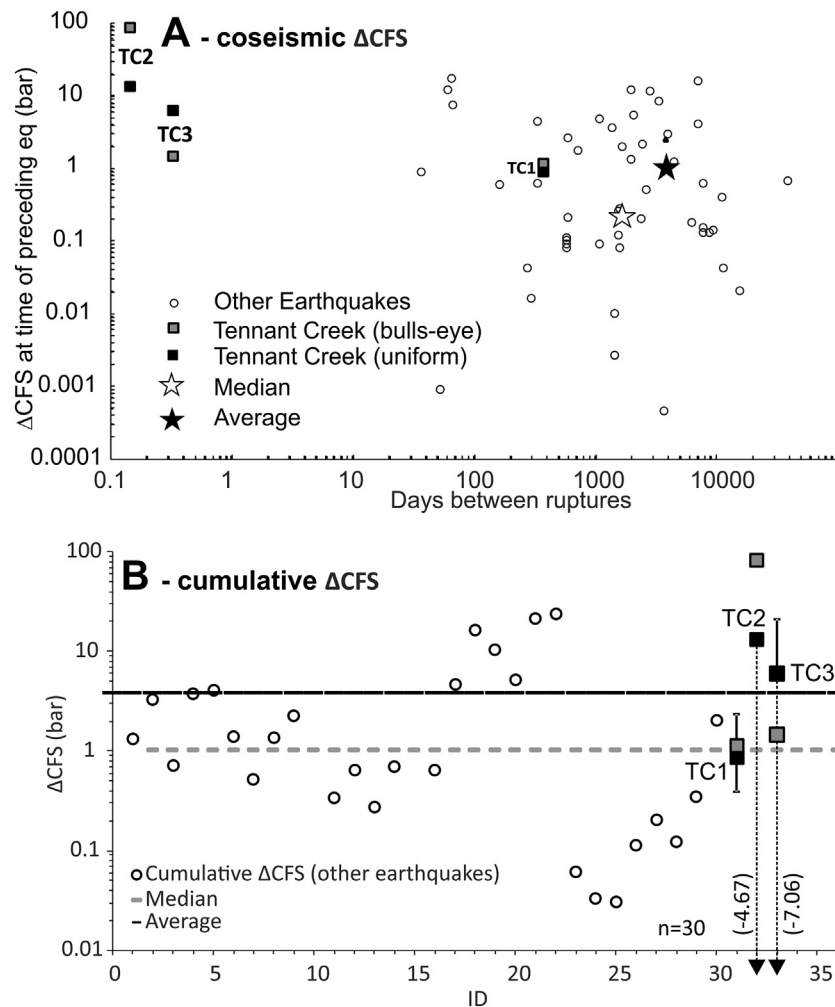


Fig. 8. A) Correlation between coseismic Δ CFS (sequence model #5 (black squares are for uniform slip and gray squares are for bulls-eye slip distribution) and time between source and receiver fault ruptures. B) Cumulative (coseismic, postseismic and interseismic) Δ CFS at receiver fault hypocentre locations immediately prior to the forthcoming earthquake (ID from Table 2 of Appendix 2).

7. Conclusions

The effects of Coulomb stress changes on the Tennant Creek earthquake sequence have been evaluated using five different planar fault source sequence models developed from different input data. Our major conclusions are:

- 1) In most fault models, for most of the major earthquakes in the Tennant Creek sequence, the hypocentral area of the forthcoming receiver fault rupture is located in an area of positive Coulomb stress loading (Δ CFS) from preceding ruptures. This suggests that Δ CFS provides a feasible mechanism for explaining many aspects of the spatiotemporal evolution of the Tennant Creek sequence, with large epistemic uncertainties in the relationships between some events resulting from different source models that produce discrepant Δ CFS values, including in some instances negative Δ CFS at receiver fault hypocentre locations.
- 2) The most refined and data-integrative model, interpreted herein to best represent the fault sources of the Tennant Creek earthquake sequence, has receiver fault Δ CFS $\geq +0.7$ to $+13$ bars at distances of ≤ 2 km of impending receiver fault hypocentres and large (≥ 30 to 99%) areas of positive Δ CFS. This highlights how progressive increases in knowledge (i.e., reduction of epistemic uncertainty) of source fault geometries may increase confidence in evaluating the role Δ CFS in influencing spatiotemporal aspects of an earthquake

sequence.

- 3) Δ CFS values estimated for the Tennant Creek earthquakes prior to impending ruptures (i.e. static stress ‘triggering’ thresholds) are at the high-end of analogous ‘threshold’ Δ CFS data estimated from other events globally (average = 3.71 bar, median = 1 bar). We speculate that the short time (hours) between Tennant Creek main shocks may relate in part to the large increase in Δ CFS on receiver faults that advanced receiver fault rupture.

Acknowledgements

This work was supported by the Australian Research Council (Discovery Grant #DP170103350). We wish to thank Kelin Wang (Editor in chief) and two anonymous reviewers for their comment and suggestions that improved the manuscript. Hiwa Mohammadi received a Baragwanath Travel Scholarship from the University of Melbourne to assist in research development.

Appendix A. Supplementary data

Supplementary data to this article can be found online at <https://doi.org/10.1016/j.tecto.2019.06.007>.

References

- Altamimi, Z., Métivier, L., Rebischung, P., Rouby, H., Collilieux, X., 2017. ITRF2014 plate motion model. *Geophys. J. Int.* 209 (3), 1906–1912.
- Avouac, J.P., Ayoub, F., Wei, S., Ampuero, J.P., Meng, L., Leprince, S., Jolivet, R., Duputel, Z., Helmberger, D., 2014. The 2013, Mw 7.7 Balochistan earthquake, energetic strike-slip reactivation of a thrust fault. *Earth Planet. Sci. Lett.* 391, 128–134.
- Beavan, J., Motagh, M., Fielding, E.J., Donnelly, N., Collett, D., 2012. Fault slip models of the 2010–2011 Canterbury, New Zealand, earthquakes from geodetic data and observations of postseismic ground deformation. *N. Z. J. Geol. Geophys.* 55 (3), 207–221.
- Belardinelli, M.E., Bizzarri, A., Cocco, M., 2003a. Earthquake triggering by static and dynamic stress changes. *Journal of Geophysical Research: Solid Earth* 108 (B3).
- Belardinelli, M.E., Sandri, L., Baldi, P., 2003b. The major event of the 1997 Umbria–Marche (Italy) sequence: what could we learn from DInSAR and GPS data? *Geophys. J. Int.* 153 (1), 242–252.
- Biasi, G.P., Wesnousky, S.G., 2016. Steps and gaps in ground ruptures: empirical bounds on rupture propagation. *Bull. Seismol. Soc. Am.* 106 (3), 1110–1124.
- Bowman, J.R., 1988. Constraints on locations of large intraplate earthquakes in the Northern Territory, Australia from observations at the Warramunga seismic array. *Geophys. Res. Lett.* 15 (13), 1475–1478.
- Bowman, J.R., 1991. Geodetic evidence for conjugate faulting during the 1988 Tennant Creek, Australia earthquake sequence. *Geophys. J. Int.* 107 (1), 47–56.
- Bowman, J.R., 1992. The 1988 Tennant Creek, northern territory, earthquakes: A synthesis. *Aust. J. Earth Sci.* 39 (5), 651–669.
- Bowman, J.R., Dewey, J.W., 1991. Relocation of teleseismically recorded earthquakes near Tennant Creek, Australia: implications for midplate seismogenesis. *Journal of Geophysical Research: Solid Earth* 96 (B7), 11973–11979.
- Bowman, J.R., Gibson, G., Jones, T., 1990a. Aftershocks of the 1988 January 22 Tennant Creek, Australia intraplate earthquakes: evidence for a complex thrust-fault geometry. *Geophys. J. Int.* 100 (1), 87–97.
- Bowman, J.R., Collins, J.A., Bostock, M.G., Grant, J., Bowman, C.C., 1990b. The Ayers Rock, Australia, earthquake of 28 May 1989: a temporally isolated mb 5.8 intraplate event. *Bull. Seismol. Soc. Am.* 80 (2), 313–324.
- Choy, G.L., Bowman, J.R., 1990. Rupture process of a multiple main shock sequence: analysis of teleseismic, local, and field observations of the Tennant Creek, Australia, earthquakes of January 22, 1988. *Journal of Geophysical Research: Solid Earth* 95 (B5), 6867–6882.
- Clark, D., McPherson, A., Van Dissen, R., 2012. Long-term behaviour of Australian stable continental region (SCR) faults. *Tectonophysics* 566, 1–30.
- Clark, D., McPherson, A., Allen, T.I., De Kool, M., 2014. Coseismic surface deformation caused by the 23 March 2012 Mw 5.4 Ernabella (Pukatja) earthquake, central Australia: implications for fault scaling relations in cratonic settings. *Bull. Seismol. Soc. Am.* 104, 24–39. <https://doi.org/10.1785/0120120361>.
- Cocco, M., Rice, J.R., 2002. Pore pressure and poroelasticity effects in Coulomb stress analysis of earthquake interactions. *Journal of Geophysical Research: Solid Earth* 107 (B2), ESE-2.
- Crone, A.J., Machette, M.N., Bowman, J.R., 1992. Geological Investigations of the 1988 Tennant Creek, Australia, Earthquakes; Implications for Paleoseismicity in Stable Continental Regions (No. 2032-A).
- Crone, A.J., Machette, M.N., Bowman, J.R., 1997. Episodic nature of earthquake activity in stable continental regions revealed by palaeoseismicity studies of Australian and North American Quaternary faults. *Aust. J. Earth Sci.* 44 (2), 203–214.
- Elliott, J.R., Nissen, E.K., England, P.C., Jackson, J.A., Lamb, S., Li, Z., Oehlers, M., Parsons, B., 2012. Slip in the 2010–2011 Canterbury earthquakes, New Zealand. *Journal of Geophysical Research: Solid Earth* 117 (B3).
- Felzer, K.R., Brodsky, E.E., 2005. Testing the stress shadow hypothesis. *Journal of Geophysical Research: Solid Earth* 110 (B5).
- Felzer, K.R., Brodsky, E.E., 2006. Decay of aftershock density with distance indicates triggering by dynamic stress. *Nature* 441 (7094), 735.
- Fletcher, J.M., Oskin, M.E., Teran, O.J., 2016. The role of a keystone fault in triggering the complex El Mayor–Cucupah earthquake rupture. *Nat. Geosci.* 9 (4), 303.
- Freed, A.M., 2005. Earthquake triggering by static, dynamic, and postseismic stress transfer. *Annu. Rev. Earth Planet. Sci.* 33, 335–367.
- Freed, A.M., Lin, J., 2001. Delayed triggering of the 1999 Hector Mine earthquake by viscoelastic stress transfer. *Nature* 411 (6834), 180.
- Gomberg, J., Reasenber, P.A., Bodin, P.L., Harris, R.A., 2001. Earthquake triggering by seismic waves following the Landers and Hector Mine earthquakes. *Nature* 411 (6836), 462.
- Green, R.G., Greenfield, T., White, R.S., 2015. Triggered earthquakes suppressed by an evolving stress shadow from a propagating dyke. *Nat. Geosci.* 8 (8), 629–632.
- Hamlin, L.J., Hreinsdóttir, S., Clark, K., Elliott, J., Liang, C., Fielding, E., Litchfield, N., Villamor, P., Wallace, L., Wright, T.J., D'Anastasio, E., 2017. Complex multifault rupture during the 2016 M w 7.8 Kaikōura earthquake, New Zealand. *Science* 356 (6334) (p.eaam7194).
- Harris, R.A., 1998. Introduction to special section: stress triggers, stress shadows, and implications for seismic hazard. *Journal of Geophysical Research: Solid Earth* 103 (B10), 24347–24358.
- Harris, R.A., Simpson, R.W., 1998. Suppression of large earthquakes by stress shadows: a comparison of Coulomb and rate-and-state failure. *Journal of Geophysical Research: Solid Earth* 103 (B10), 24439–24451.
- Harris, R.A., Simpson, R.W., 2002. The 1999 M w 7.1 Hector Mine, California, earthquake: a test of the stress shadow hypothesis. *Bull. Seismol. Soc. Am.* 92 (4), 1497–1512.
- Harris, R.A., Simpson, R.W., Reasenber, P.A., 1995. Influence of static stress changes on earthquake locations in southern California. *Nature* 375 (6528), 221.
- Hillis, R.R., Sandiford, M., Reynolds, S.D., Quigley, M.C., 2008. Present-day stresses, seismicity and Neogene-to-Recent tectonics of Australia's 'passive' margins: intraplate deformation controlled by plate boundary forces. *Geol. Soc. Lond., Spec. Publ.* 306 (1), 71–90.
- Jones, T.D., Gibson, G., McCue, K.F., Denham, D., Gregson, P.J., Bowman, J.R., 1991. Three large intraplate earthquakes near Tennant Creek, Northern Territory, on 22 January 1988. *BMR J. Aust. Geol. Geophys.* 12, 339–343.
- Kilb, D., Gomberg, J., Bodin, P., 2000. Triggering of earthquake aftershocks by dynamic stresses. *Nature* 408 (6812), 570.
- King, G.C.P., Cocco, M., 2001. Fault interaction by elastic stress changes: new clues from earthquake sequences. In: *Advances in Geophysics*. vol. 44. Elsevier, pp. 1–VIII.
- King, G.C.P., Devès, M.H., 2015. Fault Interaction, Earthquake Stress Changes, and the Evolution of Seismicity.
- King, G.C., Stein, R.S., Lin, J., 1994. Static stress changes and the triggering of earthquakes. *Bull. Seismol. Soc. Am.* 84 (3), 935–953.
- King, T.R., Quigley, M.C., Clark, D., 2018. Earthquake environmental effects produced by the Mw 6.1, 20th May 2016 Petermann earthquake, Australia. *Tectonophysics* 747, 357–372.
- Lasocki, S., Karakostas, V.G., Papadimitriou, E.E., 2009. Assessing the role of stress transfer on aftershock locations. *Journal of Geophysical Research: Solid Earth* 114 (B11).
- Leonard, M., 2014. Self-consistent earthquake fault-scaling relations: update and extension to stable continental strike-slip faults. *Bull. Seismol. Soc. Am.* 104 (6), 2953–2965.
- Leonard, M., Ripper, I.D., Yue, L., 2002. Australian earthquake fault plane solutions: geoscience Australia. *Record* 2002 (19).
- Lin, J., Stein, R.S., 2004. Stress triggering in thrust and subduction earthquakes and stress interaction between the southern San Andreas and nearby thrust and strike-slip faults. *Journal of Geophysical Research: Solid Earth* 109 (B2).
- McCaffrey, R., 1989. Teleseismic investigation of the January 22, 1988 Tennant Creek, Australia, earthquakes. *Geophys. Res. Lett.* 16 (5), 413–416.
- Meier, M.A., Werner, M.J., Woessner, J., Wiemer, S., 2014. A search for evidence of secondary static stress triggering during the 1992 Mw7. 3 Landers, California, earthquake sequence. *Journal of Geophysical Research: Solid Earth* 119 (4), 3354–3370.
- Mildon, Z.K., Toda, S., Faure Walker, J.P., Roberts, G.P., 2016. Evaluating models of Coulomb stress transfer: is variable fault geometry important? *Geophys. Res. Lett.* 43 (24).
- Mildon, Z.K., Roberts, G.P., Faure Walker, J.P., Iezzi, F., 2017. Coulomb stress transfer and fault interaction over millennia on non-planar active normal faults: the M w 6.5–5.0 seismic sequence of 2016–2017, central Italy. *Geophys. J. Int.* 210 (2), 1206–1218.
- Mildon, Z., Roberts, G., Walker, J.F., Toda, S., 2018. Coulomb Pre-stress and Fault Bends: Ignored Yet Vital Factors for Earthquake Triggering. <https://eartharxiv.org/pt829>.
- Mohammadi, H., Bayrak, Y., 2015. The M w 6.3 Shonbeh (Bushehr) mainshock, and its aftershock sequence: Tectonic implications and seismicity triggering. *Eastern Anatolian Journal of Science* 1 (2), 43–56.
- Mohammadi, H., Bayliss, T.J., Ghachkanlu, E.N., 2017. Seismogenesis and earthquake triggering during the 2010–2011 Rigan (Iran) earthquake sequence. *J. Afr. Earth Sci.* 126, 84–95.
- Nissen, E., Elliott, J.R., Sloan, R.A., Craig, T.J., Funning, G.J., Hutko, A., Parsons, B.E., Wright, T.J., 2016. Limitations of rupture forecasting exposed by instantaneously triggered earthquake doublet. *Nat. Geosci.* 9 (4), 330.
- Nostro, C., Cocco, M., Belardinelli, M.E., 1997. Static stress changes in extensional regimes: an application to southern Apennines (Italy). *Bull. Seismol. Soc. Am.* 87 (1), 234–248.
- Okada, Y., 1992. Internal deformation due to shear and tensile faults in a half-space. *Bull. Seismol. Soc. Am.* 82 (2), 1018–1040.
- Pollitz, F.F., 1997. Gravitational viscoelastic postseismic relaxation on a layered spherical Earth. *Journal of Geophysical Research: Solid Earth* 102 (B8), 17921–17941.
- Pollitz, F.F., Wicks, C., Thatcher, W., 2001. Mantle flow beneath a continental strike-slip fault: postseismic deformation after the 1999 Hector Mine earthquake. *Science* 293 (5536), 1814–1818.
- Pollitz, F.F., Stein, R.S., Sevilgen, V., Bürgmann, R., 2012. The 11 April 2012 east Indian Ocean earthquake triggered large aftershocks worldwide. *Nature* 490 (7419), 250.
- Quigley, M.C., Cupper, M.L., Sandiford, M., 2006. Quaternary faults of south-central Australia: palaeoseismicity, slip rates and origin. *Aust. J. Earth Sci.* 53 (2), 285–301.
- Quigley, M.C., Clark, D., Sandiford, M., 2010. Tectonic geomorphology of Australia. *Geol. Soc. Lond., Spec. Publ.* 346 (1), 243–265.
- Quigley, M.C., Jiménez, A., Duffy, B., King, T.R., 2019. Physical and Statistical Behavior of Multifault Earthquakes: Darfield Earthquake Case Study, New Zealand. *J. Geophys. Res.: Solid Earth*.
- Rajabi, M., Tingay, M., Heidbach, O., Hillis, R., Reynolds, S., 2017. The Present-day stress field of Australia. *Earth Sci. Rev.* 168, 165–189.
- Reasenber, P.A., Simpson, R.W., 1992. Response of regional seismicity to the static stress change produced by the Loma Prieta earthquake. *Science* 255 (5052), 1687–1690.
- Rybicki, K., 1973. Analysis of aftershocks on the basis of dislocation theory. *Phys. Earth Planet. Inter.* 7 (4), 409–422.
- Scholz, C.H., 2010. Large earthquake triggering, clustering, and the synchronization of faults. *Bull. Seismol. Soc. Am.* 100 (3), 901–909.
- Sieh, K., Jones, L., Hauksson, E., Hudnut, K., Eberhart-Phillips, D., Heaton, T., Hough, S., Hutton, K., Kanamori, H., Lilje, A., Lindvall, S., 1993. Near-field investigations of the Landers earthquake sequence, April to July 1992. *Science* 260 (5105), 171–176.
- Skempton, A.W., 1954. The pore-pressure coefficients A and B. *Geotechnique* 4 (4), 143–147.

- Smith, S.W., Van de Lindt, W., 1969. Strain adjustments associated with earthquakes in southern California. *Bull. Seismol. Soc. Am.* 59 (4), 1569–1589.
- Steacy, S., Gombert, J., Cocco, M., 2005. Introduction to special section: stress transfer, earthquake triggering, and time-dependent seismic hazard. *Journal of Geophysical Research: Solid Earth* 110 (B5).
- Steacy, S., Jiménez, A., Holden, C., 2013. Stress triggering and the Canterbury earthquake sequence. *Geophys. J. Int.* 196 (1), 473–480.
- Steacy, S., Gerstenberger, M., Williams, C., Rhoades, D., Christophersen, A., 2014. A new hybrid Coulomb/statistical model for forecasting aftershock rates. *Geophys. J. Int.* 196 (2), 918–923.
- Stein, R.S., 1999. The role of stress transfer in earthquake occurrence. *Nature* 402 (6762), 605.
- Stein, R.S., King, G.C., Lin, J., 1994. Stress triggering of the 1994 M = 6.7 Northridge, California, earthquake by its predecessors. *Science* 265 (5177), 1432–1435.
- Stein, R.S., Barka, A.A., Dieterich, J.H., 1997. Progressive failure on the North Anatolian fault since 1939 by earthquake stress triggering. *Geophys. J. Int.* 128 (3), 594–604.
- Toda, S., Stein, R., 2003. Toggling of seismicity by the 1997 Kagoshima earthquake couplet: a demonstration of time-dependent stress transfer. *Journal of Geophysical Research: Solid Earth* 108 (B12).
- Toda, S., Stein, R.S., Richards-Dinger, K., Bozkurt, S.B., 2005. Forecasting the evolution of seismicity in southern California: animations built on earthquake stress transfer. *Journal of Geophysical Research: Solid Earth* 110 (B5).
- Toda, S., Stein, R.S., Sevilgen, V., Lin, J., 2011. Coulomb 3.3 graphic-rich deformation and stress-change software for earthquake, tectonic, and volcano research and teaching-user guide (no. 2011-1060). US Geological Survey.
- Tregoning, P., 2002. Plate kinematics in the western Pacific derived from geodetic observations. *Journal of Geophysical Research: Solid Earth* 107 (B1), ECV-7.
- Van Der Elst, N.J., Brodsky, E.E., 2010. Connecting near-field and far-field earthquake triggering to dynamic strain. *Journal of Geophysical Research: Solid Earth* 115 (B7).
- Verdecchia, A., Pace, B., Visini, F., Scotti, O., Peruzza, L., Benedetti, L., 2018. The role of viscoelastic stress transfer in long-term earthquake cascades: insights after the central Italy 2016–2017 seismic sequence. *Tectonics* 37 (10), 3411–3428.
- Walters, R.J., Gregory, L.C., Wedmore, L.N.J., Craig, T.J., McCaffrey, K., Wilkinson, M., Chen, J., Li, Z., Elliott, J.R., Goodall, H., Iezzi, F., 2018. Dual control of fault intersections on stop-start rupture in the 2016 Central Italy seismic sequence. *Earth Planet. Sci. Lett.* 500, 1–14.
- Wang, J., Xu, C., Freymueller, J.T., Li, Z., Shen, W., 2014. Sensitivity of Coulomb stress change to the parameters of the Coulomb failure model: a case study using the 2008 Mw 7.9 Wenchuan earthquake. *Journal of Geophysical Research: Solid Earth* 119 (4), 3371–3392.
- Wedmore, L.N.J., Walker, J.F., Roberts, G.P., Sammonds, P.R., McCaffrey, K.J.W., Cowie, P.A., 2017. A 667-year record of coseismic and interseismic Coulomb stress changes in central Italy reveals the role of fault interaction in controlling irregular earthquake recurrence intervals. *Journal of Geophysical Research: Solid Earth* 122 (7), 5691–5711.
- Wei, S., Fielding, E., Leprince, S., Sladen, A., Avouac, J.P., Helmberger, D., Hauksson, E., Chu, R., Simons, M., Hudnut, K., Herring, T., 2011. Superficial simplicity of the 2010 El Mayor-Cucapah earthquake of Baja California in Mexico. *Nat. Geosci.* 4 (9), 615–618.
- Wesnousky, S.G., 2008. Displacement and geometrical characteristics of earthquake surface ruptures: issues and implications for seismic-hazard analysis and the process of earthquake rupture. *Bull. Seismol. Soc. Am.* 98 (4), 1609–1632.
- Woessner, J., Jonsson, S., Sudhaus, H., Baumann, C., 2012. Reliability of Coulomb stress changes inferred from correlated uncertainties of finite-fault source models. *Journal of Geophysical Research: Solid Earth* 117 (B7).
- Zhan, Z., Jin, B., Wei, S., Graves, R.W., 2011. Coulomb stress change sensitivity due to variability in mainshock source models and receiving fault parameters: a case study of the 2010–2011. Christchurch, New Zealand, earthquakes. *Seismol. Res. Lett.* 82 (6), 800–814.